Steady and unsteady numerical simulations of the flow in the Tokke Francis turbine model, at three operating conditions

2015 J. Phys.: Conf. Ser. 579 012011

(http://iopscience.iop.org/1742-6596/579/1/012011)

Journal of Physics: Conference Series **579** (2015) 012011 doi:10.1088/1742-6596/579/1/012011

Steady and unsteady numerical simulations of the flow in the Tokke Francis turbine model, at three operating conditions

Lucien Stoessel[1], **Håkan Nilsson**[2]

[1] Master's student, Laboratory for Hydraulic Machines, École polytechnique fédérale de Lausanne, CH-1015 Lausanne, Switzerland

[2] Professor, Division of Fluid Dynamics, Department of Applied Mechanics, Chalmers University of Technology, SE-41296 Gothenburg, Sweden

E-mail: [1] lucien.stoessel@alumni.epfl.ch, [2] hakan.nilsson@chalmers.se

Abstract. This work investigates the flow in the scale model of the high-head Tokke Francis turbine at part load, best efficiency point and high load, as a contribution to the first Francis-99 workshop. The work is based on the FOAM-extend CFD software, which is a recent fork of the OpenFOAM CFD software that contains new features for simulations in rotating machinery. Steady-state mixing plane RANS simulations are conducted, with an inlet before the guide vanes and an outlet after the draft tube. Different variants of the k-ε and k-ω turbulence models are used and a linear explicit algebraic Reynolds stress model is implemented. Sliding grid URANS simulations, using a general grid interface coupling, are performed including the entire turbine geometry, from the inlet to the spiral casing to the outlet of the draft tube. For the unsteady simulations, the k-ω SSTF model is implemented and used in addition to the standard k-ε model. Both the steady and unsteady simulations give good predictions of the pressure distribution in the turbine compared to the experimental results. The velocity profiles at the runner outlet are well predicted at off-design conditions. A strong swirl is however obtained at best efficiency point, which is not observed in the experiments. While the steady-state simulations strongly overestimate the efficiency, the unsteady simulations give good predictions at best efficiency point (error of 1.16%) with larger errors at part load (10.67%) and high load (2.72%). Through the use of Fourier decomposition, the pressure fluctuations in the turbine are analysed, and the main rotor-stator interaction frequencies are predicted correctly at all operating conditions.

1. Introduction

Water turbines are often used to regulate the electric grid - to balance electricity demand and supply - since they are able to change operating point within a short time frame [1]. This requires the turbines to frequently run at off-design conditions and during transients between different operating conditions. The turbines are traditionally designed for steady operation at a single operating point, which is characterised by a stable flow with minimal swirl at the turbine outlet. In contrast, off-design operation lead to more complex flow through the turbine and the creation of a swirl at the runner outlet [2]. Such unsteady flow features can lead to fluid-structure interaction phenomena and oscillating forces on the runner [3, 4]. It is therefore of importance to investigate the flow in water turbines both at best efficency point and at off-design points. The turbines should be designed to give a high efficiency and to avoid unstable

conditions. Validated numerical results can be used to extend the knowledge of the flow in the turbines, and to improve turbine design.

The present work uses the FOAM-extend fork of the OpenFOAM CFD software to study the flow in the Tokke high-head Francis turbine model (Francis-99). FOAM-extend was referred to as OpenFOAM-dev and OpenFOAM-ext in previous work. The FOAM-extend software and its tools for turbomachinery simulations have been validated and applied on hydro-power simulation cases by Nilsson [5], Petit [6] and Javadi [7]. Features for steady-state turbomachinery simulations were developed by Beaudoin *et al.* [8], and tested by Page *et al.* [9]. Petit *et al.* [10] set up an open case study that proved the validity of FOAM-extend for unsteady sliding grid simulations of swirling flows. Zhang and Zhang [11] used OpenFOAM on high-head Francis turbines, and included a model for cavitation. Recent work on Francis turbines at off-design conditions using proprietary software was performed by Nicolet *et al.* [4] for part load and by Shingai *et al.* [2] for high load operation. Susan-Resiga *et al.* [12] also included efforts to reduce the computational effort by the use of symmetry assumptions. The use of different turbulence models for RANS simulations of Francis turbines was investigated and compared to experiments at best efficiency point by Maruzewski *et al.* [13], while Wu *et al.* [14] validated their turbulence model in various operating conditions.

The present work examines the flow in the Tokke high-head Francis turbine model at best efficiency point, part load and high load using several turbulence models and using two rotor-stator-interaction approaches. Steady-state simulations are performed using a single guide vane and runner blade passage, and a mixing plane coupling between the stationary and rotating parts of the domain. Unsteady simulations are performed using all the blade passages and a sliding general grid interface (GGI). The steady-state simulations include the guide vane passage, the runner, and the draft tube. The unsteady simulations also include the spiral casing and the stay vanes. The pressure and velocity distributions are compared with the experimental and numerical results by Trivedi *et al.* [15], and additional experimental data that was distributed before the first Francis-99 workshop (www.francis-99.org).

2. Case description and numerical details

This section gives a brief description of the Tokke Francis turbine model case, and the numerical set-up used in the present work.

2.1. Turbine description and operating points

The Tokke turbine is a high-head Francis turbine with 15 full-length runner blades and 15 splitter blades, with a distributor consisting of 14 stay-vanes and 28 guide-vanes. The prototype has a runner outlet diameter $D = 1.779m$, a rated head of $H = 377m$ and a rated output power of $110MW$. The model turbine, studied in the present work, has a runner outlet diameter $D = 0.349m$ and a rated head of $H = 12m$. A cut view of the entire turbine geometry with all the components is shown in Figure 1. The turbine is limited by the inlet section I at the inlet of the spiral casing, and the outlet section $\bar{I}$ at the draft tube outlet. Three different operating points are examined; part load, best efficiency point and high load. A summary of the operating conditions is shown in Table 1. Due to experimental flow instabilities, the data for the best efficiency and high load conditions were given at two slightly different conditions, by the Francis-99 workshop organizers. The present steady-state simulations are therefore conducted at the three initial operating points, as well as the two additional operating points at best efficiency and high load. Due to the large computational cost, the unsteady simulations are only conducted at the initial conditions that were suggested at the time of those simulations. The velocity distributions of the unsteady results are thus compared with the experimental results at slightly different conditions.

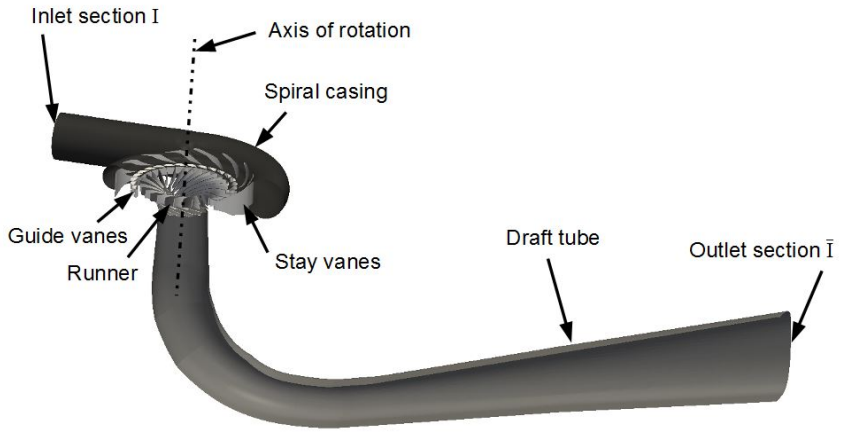

Figure 1: Cut view of the entire turbine geometry.

Parameter	Part load	BEP 1	BEP 2	High load 1	High load 2
$H\ [m]$	12.29	11.91	12.77	11.84	12.61
$Q\ [m^3/s]$	0.071	0.203	0.21	0.221	0.23
$n\ [rpm]$	406.2	335.4	344.4	369.6	380.4
$\eta_{h,F99} = \omega T/(\rho Q \Delta p_0)[-]$	71.69	92.61	92.4	90.66	91.0

Table 1: Physical parameters for all operating points. BEP 2 and high load 2 correspond to the velocity measurements close to the original BEP 1 and high load 1 conditions, and are therefore used for the comparison of the velocity profiles.

It should be noted that in Table 1, the definition of the hydraulic efficiency neglects the potential energy. Here Δp_0 is the difference in total pressure between the inlet section I and the outlet section $\bar{I}$, given by

$$\Delta p_0 = p_{0,I} - p_{0,\bar{I}} = p_I - p_{\bar{I}} + \frac{\rho Q^2}{2} \cdot \left(\frac{1}{A_I^2} - \frac{1}{A_{\bar{I}}^2}\right). \tag{1}$$

This expression is not consistent with the definition in the IEC standard [16], which includes the gravitational term.

2.2. Mesh and boundary conditions

Original block-structured hexahedral meshes were supplied by the workshop organizers. Due to some severe imperfections, they were slightly improved in the present work. A detailed description of the mesh modifications is given in the Master's thesis by Stoessel. The meshes were also adapted for the different types of simulations. The steady-state mixing plane simulations are conducted for one guide vane passage and one blade channel, and the complete draft tube, as seen in Figure 2. The inlet boundary condition is set at the inlet of the guide vane passage. The inlet radial velocity is given by the flow rate and the inlet cross-sectional area. The inlet tangential velocity is given by a ratio of $\frac{U_R}{U_\theta} = \frac{2}{3}$ between the radial and tangential components, approximating the angle of the stay vanes. The inlet turbulence is specified by a turbulence intensity of 10%, and a ratio between the turbulent and laminar viscosities of $\nu_t/\nu = 10$. At the draft tube outlet the static pressure is set to zero, and a zero gradient boundary condition is applied for the other variables. A mixing plane interface is used at the runner inlet and outlet, yielding a circumferential average of the flow field [9] at those interfaces. A refined mesh is used

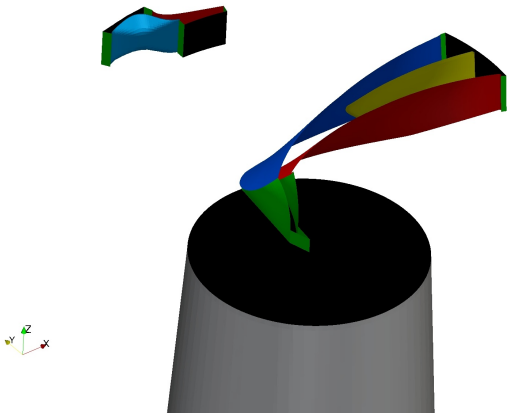

Figure 2: Computational domain for the steady-state simulations.

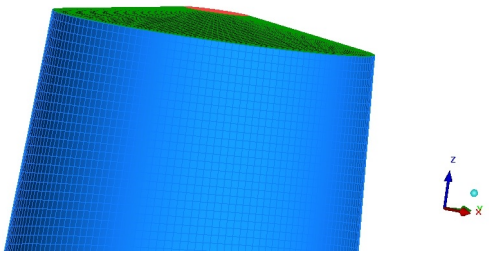

Figure 3: New shape of the interface between runner and draft tube, for the unsteady simulations. Originally flat, now conical.

for the best efficiency point, with improvements in the region below the hub and between the guide vanes. The off-design meshes are kept similar as the distributed meshes, except for the most important improvements. The resulting meshes contain 3,947,947 cells at best efficiency point, 3,931,653 at high load and 3,929,101 at part load.

The entire turbine geometry is used in the unsteady simulations, as seen in Figure 1. The boundary conditions are set as for the steady-state cases except that the velocity is specified normal to the inlet boundary. The mesh topology at the runner outlet is modified and the flat interface between the runner outlet and the draft tube inlet is replaced by a conical surface, as seen in Figure 3. This improves the mesh quality in the region below the hub. A general grid interface (GGI) [17] is used for the coupling between the rotating and stationary parts, allowing the use of a sliding grid method with non-conformal meshes. The meshes consist of 12,214,685 cells for the best efficiency point, 12,357,362 for the high load point, and 12,709,257 for the part load point. The supplied spiral casing and stay vane mesh has severe quality issues that affect the pressure convergence and should be solved in the future by re-meshing this region.

2.3. Numerical method

The software used for the simulations is FOAM-extend-3.0-Turbo, which is a modified version of FOAM-extend-3.0. It includes recent turbomachinery-specific developments, such as an improved implementation of the mixing plane interface. The code is based on the finite volume method, and the pressure-velocity coupling is handled using the SIMPLE algorithm in all the present simulations. The convection terms are discretised with a second-order linear upwind scheme.

For the steady-state simulations, a solver that uses multiple rotating frames of references (MRF) is chosen to mimic the behaviour of a rotating runner. A mixing plane is applied between stationary and rotating parts of the domain. Different schemes are available in FOAM-extend-3.0-Turbo to link the flow variables on either side of the mixing plane interface. For the best efficiency point simulations, the fluxAveragingAdjustMassFlow scheme is used for the velocity, where the values are adjusted to guarantee a conserved mass flow. A scheme based on a zero gradient boundary condition, preserving a corrrect mean value, called zeroGradientAreaAveragingMix is used for the pressure. At off-design, the default areaAveraging scheme is used for all variables. All variables are solved with a stabilised bi-conjugate gradient method and a diagonal incomplete LU-decomposition for preconditioning.

The unsteady simulations are performed with a solver that allows a physical rotation of the rotating part of the domain, and a coupling between the stationary and rotating parts of the domain with a GGI interface. The pressure is solved with a conjugate gradient method and diagonal incomplete Cholesky preconditioning, while the other variables are solved using a bi-conjugate gradient method with diagonal incomplete LU-decomposition for preconditioning. The time step corresponds to 0.25° of runner rotation, yielding maximum CFL numbers of about 4.5, 2.85 and 2.27 for best efficiency, part load and high load, respectively.

2.4. Turbulence models

The turbulence models used for steady-state simulations are the standard k-ε, RNG k-ε, realizable k-ε and k-ω SST. In addition, the linear explicit algebraic Reynolds stress model (EARSM) proposed by Wallin [18, paper 6, 196-199] was implemented and tested. For the unsteady simulations, the standard k-ε and the k-ω SSTF model developed by Gyllenram and Nilsson [19] are compared. All of the turbulence models use standard high-Reynolds wall functions.

3. Results

The results are here evaluated, based on the hydraulic efficiency, the static pressure and velocity distributions, and the pressure and torque fluctuations.

3.1. Hydraulic efficiency

Figure 4 compares the hydraulic efficiency of both the steady and unsteady simulations with the experimental and numerical results by Trivedi *et al.* [15]. While both of the present unsteady simulations give good agreement with the experimental data at best efficiency point, yielding an error of 1.16%, the difference to the experimental data increases to 2.72% at high load and 10.67% at part load. The behaviour of the unsteady numerical results is very similar to that of the numerical results of Trivedi *et al.* [15]. The steady-state simulations, on the other hand, give a strong over-prediction of the efficiency. In addition, the steady-state peak efficiency does not occur at the same flow rate as in the experimental data. This may be due to the definition of the inlet boundary conditions at the guide vane inlet, and that the hydraulic efficiencies of the steady-state cases are directly evaluated using those conditions. An example of other possible reasons for this effect is the mixing plane. The present work uses a newly implemented mixing plane, and this is the first comparison with experimental data. There may still be some issues with the implementation, but there may as well be some fundamental issues with the mixing plane concept. A study of the exact cause of this effect is left for future work. It should be recalled that the unsteady simulations have the inlet before the spiral casing, where the flow is more well-known with less streamwise gradients.

3.2. Head and torque

Depending on the type of calculations and the turbulence models that are used, different values are obtained for the resulting hydrostatic head and the torque at the shaft (Tables 2 and 3). For simplicity, only the results obtained with the standard k-ε are shown. For steady-state simulations (Table 2), the variations of the torque with other turbulence models are within 4.4% at part load, 0.7% at best efficiency point, and 0.9% at high load. For the head, the values are within 11.8% at part load, 1.1% at best efficiency point and 1.1% at high load. The time-averaged values of the unsteady simulations (Table 3) present differences to the standard $k-\varepsilon$ results of 0.28% at part load, 4% at best efficiency point and 1.9% at high load for the torque. The values of the time-averaged head have deviations of 0.07% at part load, 9.5% at best efficiency point and 8.7% at high load.

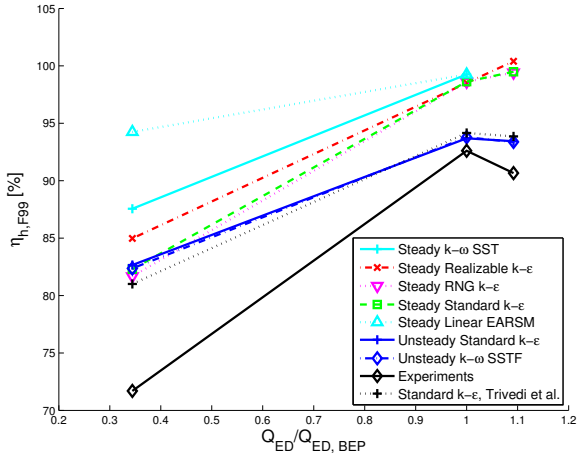

Figure 4: Hydraulic efficiency as a function of the relative unit flow rate, $Q_{ED}/Q_{ED,BEP} = (Q\sqrt{H_{BEP}})/(Q_{BEP}\sqrt{H})$.

Parameter	Part load	BEP	High load
H_{F99} $[m]$	12.47	13.148	11.01
T $[Nm]$	168.15	735.47	613.54

Table 2: Head and torque results of the steady-state standard k-ε calculations for the three original operating points.

Parameter	Part load	BEP	High load
H_{F99} $[m]$	13.78	13.87	11.99
T $[Nm]$	186.34	736.07	627.06

Table 3: Time-averaged head and torque results of the unsteady standard k-ε calculations for the three original operating points.

3.3. Static pressure distribution

Figure 5 shows the locations of the experimental static pressure probes, and 6 shows the corresponding static pressure distributions. The numerical static pressure level at the outlet of the draft tube is adjusted to that of the experiment. Those are $p_{\bar{I}} = 101.562kPa$ at best efficiency point, $p_{\bar{I}} = 99.536kPa$ at part load, and $p_{\bar{I}} = 95.977kPa$ at high load. The mixing plane simulations show good agreement with the unsteady simulations by Trivedi *et al.*, regardless of the turbulence model. The unsteady simulations give a higher static pressure on the blade suction side, while the static pressure in the vaneless space between the guide vanes and runner blades is closer to the experimental data. All the simulations predict a decrease in pressure between the $P71$ probe and the draft tube, while the experiment shows a slight increase. This indicates that certain phenomena occurring at the runner outlet are not represented the same way in the experiment and in the numerical simulations. Figure 7 gives an overview of the static pressure distribution in the symmetry plane of the draft tube. The static pressure probes, $DT11$ and $DT21$, are located on opposite walls just below the upper velocity measurement section. A significant reduction in static pressure is observed at the centerline, and its predicted width must be very important for the static pressure at the walls in that region.

Figure 8 shows that all numerical pressure distributions at part load agree to a high degree, and follow a similar trend as the experimental data. Figure 9 shows that there is no local region

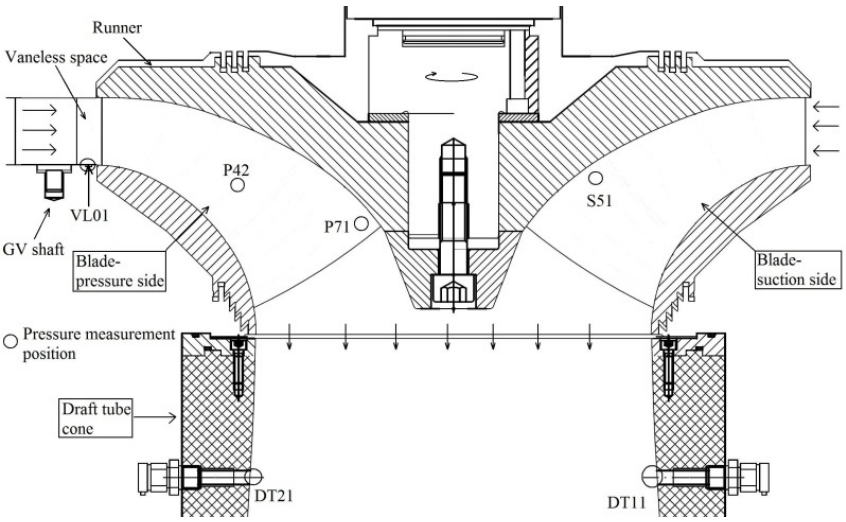

Figure 5: Locations of the static pressure probes in the guide vane cascade, runner and draft tube (illustration taken from the Francis-99 workshop website with kind permission of Prof. M.Cervantes).

of reduced pressure at the centerline in this case, and the all the numerical results do predict a similar static pressure increase between $P71$ and the draft tube probes as the experimental data.

Figure 10 shows that all numerical pressure distributions at high load are quite similar, and correspond to the experimental data except for the two probes in the draft tube. Figure 11 shows that there is again a local reduction of the static pressure at the centerline which may be a cause of the discrepancy.

The static pressure level of the numerical results is set to the same level as that of the experiment at the outlet of the draft tube. A numerical problem between probe $P71$ and the draft tube probes will thus change the level of the upstram probes accordingly. For the best efficiency and part load points, the numerically predicted static pressure at the draft tube probes correspond quite well with the experimental value, indicating that the draft tube performance is predicted reasonably well. Shifting the upstream points to lower values would in most cases improve the results. This indicates that additional attention should be paid to the numerical methods and the computational mesh in that region. On the other hand, the high load results would get worse with such an operation, although there is also a strong indication of problems in that region. The curves indicate that also the performance of the draft tube may not be predicted as well for the high load condition.

3.4. Velocity profiles

The velocity distributions in the draft tube cone were measured experimentally along two lines, located at $z = -0.2434m$ and at $z = -0.5614m$ respectively, shown as black lines in Figures 7, 9 and 11. The experimental data presented in this section corresponds to the original operating condition at part load, but to the two additional operating conditions at best efficiency and high load. The steady-state results are taken from the same conditions as the experimental data, while the unsteady results are taken from the original conditions.

Figure 12 shows the velocity distributions for the best efficiency point. All numerical results show a strong swirl near the axis of rotation which is not present in the experiments. This is related to the local reduction in the static pressure at the centerline, as discussed for Figure 7. The velocity distributions at the second measurement line shows that the swirl is

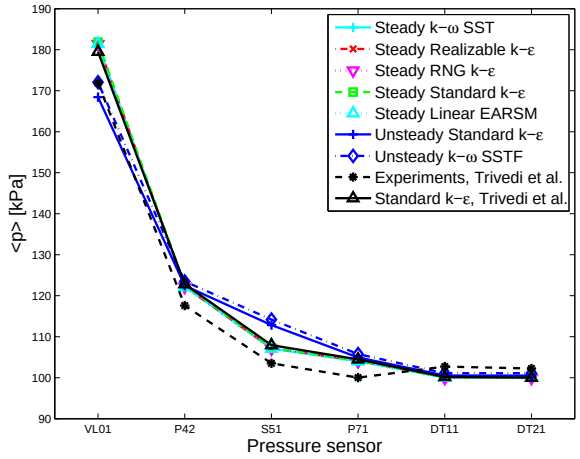

Figure 6: Static pressure distribution at best efficiency point.

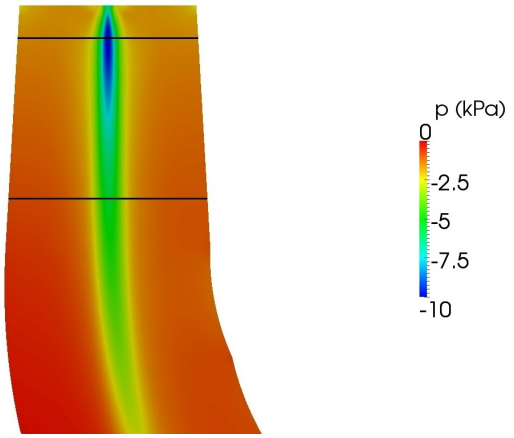

Figure 7: Static pressure distribution at the symmetry plane of the draft tube cone for a steady-state simulations at best efficiency point. The black lines indicate the location of the velocity measurement sections.

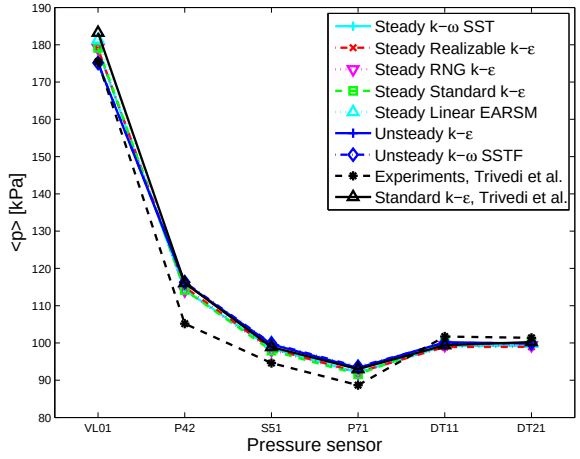

Figure 8: Static pressure distribution at part load.

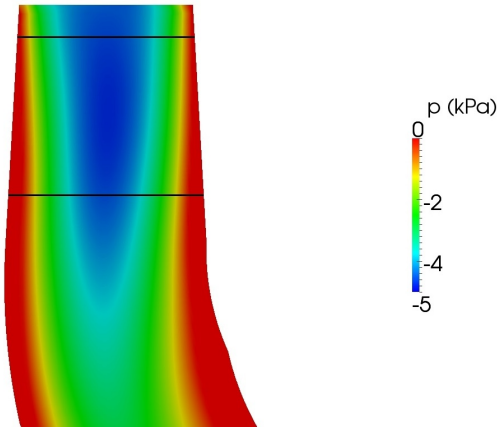

Figure 9: Static pressure distribution at the symmetry plane of the draft tube cone for a steady-state simulations at part load. The black lines indicate the location of the velocity measurement sections.

still over-predicted by the steady-state simulations, while the unsteady profile approaches the experimental data. The numerical axial velocity distributions agree well with the experimental data over most of the draft tube width, except for the region near the rotation axis. At the first line, only the unsteady standard k-ε simulation predicts the recirculation zone below the hub correctly, while it is under-predicted by the steady simulations and over-predicted by the unsteady k-ω SSTF results. All simulations strongly over-predict this wake region at the second line, especially the steady EARSM and the unsteady simulations, and only the steady realizable k-ε simulation gives a correct width of the recirculation zone at this location.

Figure 13 shows that there is a strong swirl near the draft tube walls at the part load condition.

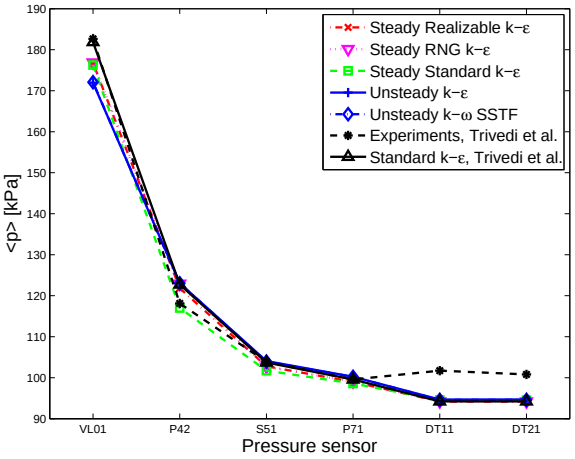

Figure 10: Static pressure distribution at high load.

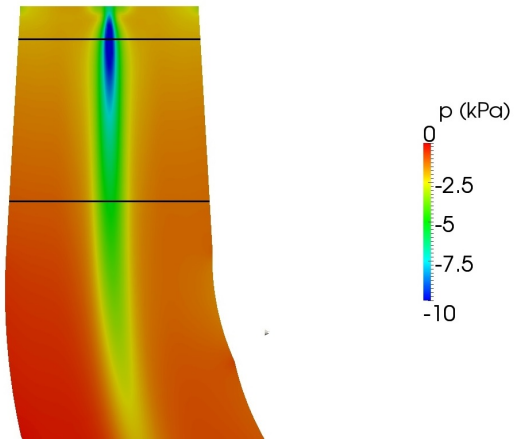

Figure 11: Static pressure distribution at the symmetry plane of the draft tube cone for a steady-state simulations at high load. The black lines indicate the location of the velocity measurement sections.

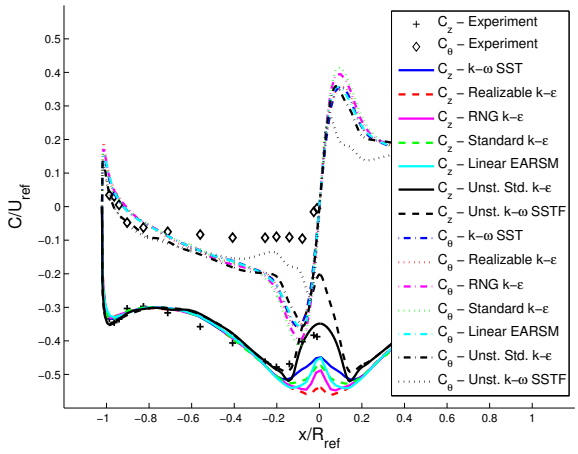

(a) Line 1.

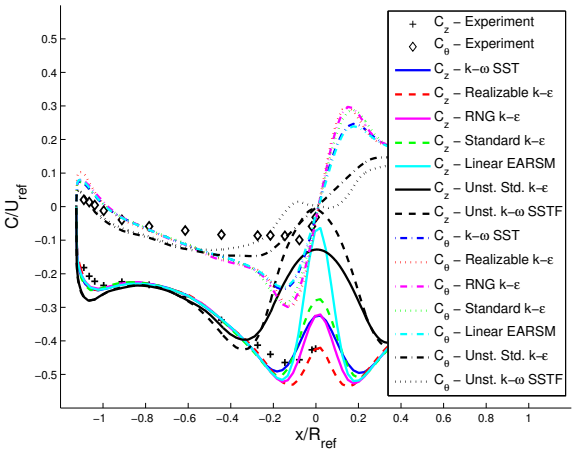

(b) Line 2.

Figure 12: Dimensionless velocity distributions in the draft tube cone at the best efficiency point. C_z: axial. C_θ: tangential. Note that the unsteady simulations were conducted at a slightly different operating condition than that of the experiment.

Most of the flow is passing in this region, while there is a stagnation with some back-flow in the rest of the cross-section. This recirculation region is clearly visible on the pressure contours in Figure 9, as a large low pressure region that extends over a large part of the draft tube width. These phenomena are well captured both by the steady and unsteady simulations. The steady k-ω SST gives the best prediction at the first line. The best agreement at the second line is given by the steady-state standard and RNG k-ε simulations, and those models give reasonable results also at the first line.

Figure 14 shows that the axial velocity distributions correspond well to the measurements in a large portion of the draft tube at high load. However, all numerical results predict a

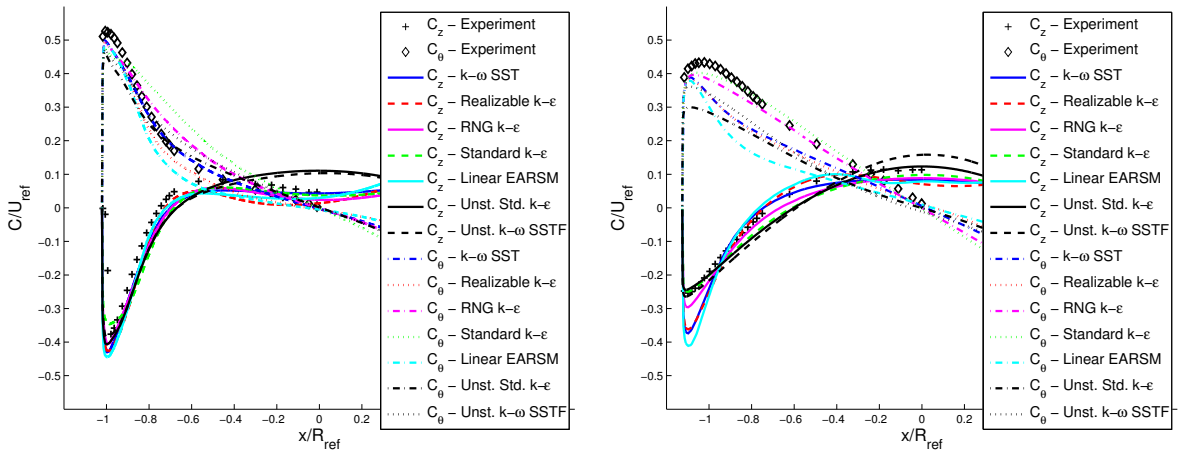

(a) Line 1. (b) Line 2.

Figure 13: Dimensionless velocity distributions in the draft tube cone at part load. C_z: axial. C_θ: tangential.

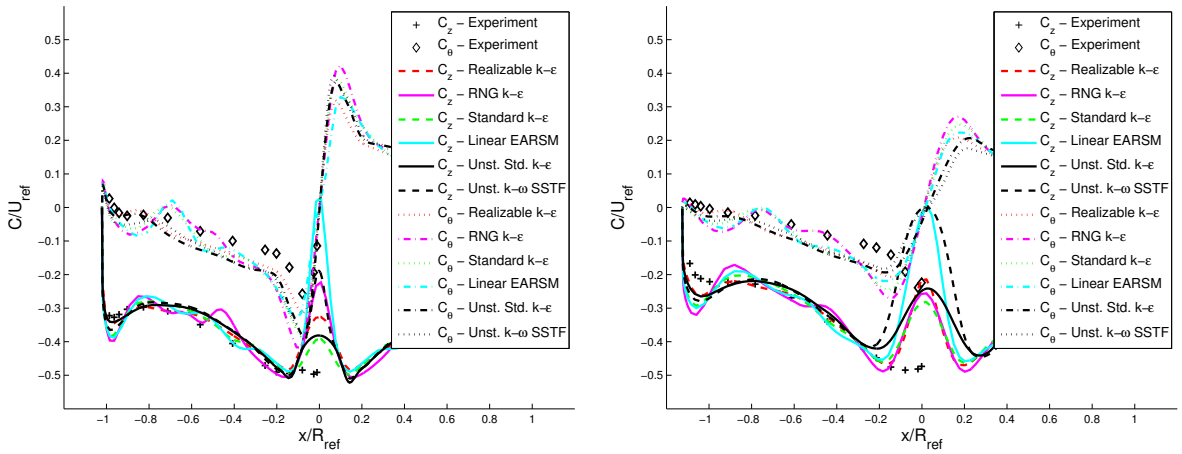

(a) Line 1. (b) Line 2.

Figure 14: Dimensionless velocity profiles in the draft tube cone at high load. C_z: axial. C_θ: tangential. Note that the unsteady simulations were conducted at a slightly different operating condition than that of the experiment.

much stronger on-axis recirculation than in the experiment. The predicted swirl behaves as the experimental, but is overestimated by all models. This swirl is then attenuated until the second measurement lines, but is still larger than the experimental one. The RNG k-ε and linear EARSM results show some unexpected variations in the radial direction, which is probably due to numerical instability.

3.5. Pressure and torque fluctuations

The pressure and torque fluctuations of the unsteady simulations are analysed using discrete fast Fourier transform. Only the results for standard k-ε are shown here. The frequency spectra of the pressure fluctuations at the best efficiency point are shown in Figure 15. The fluctuations in the vaneless space contain a frequency of $14.9n$. This is also found in the experimental results,

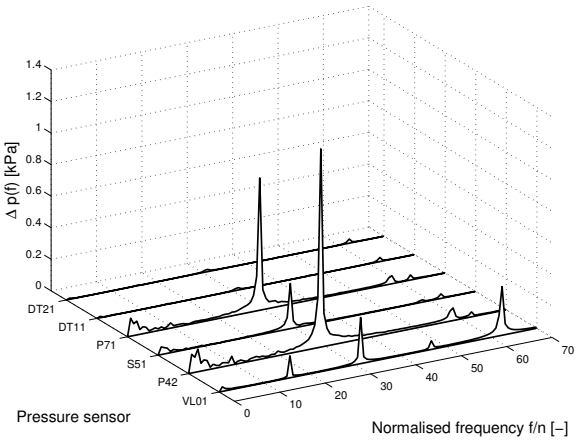

Figure 15: Frequency spectra of the pressure fluctuations at best efficiency point, normalised by the runner rotation frequency. Unsteady k-ε.

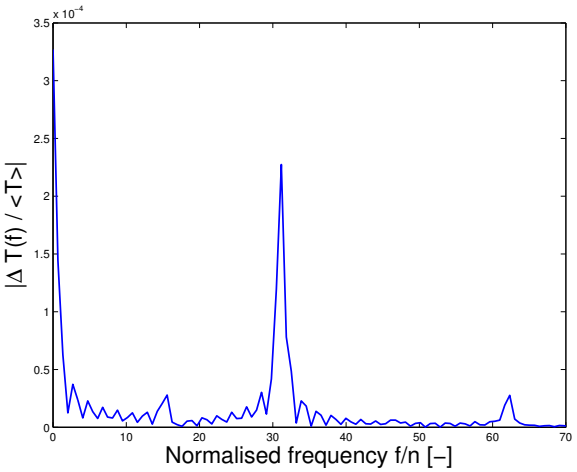

Figure 16: Frequency spectrum of the axial torque at best efficiency point, normalised by the runner rotation frequency. Unsteady k-ε.

and corresponds to the full blade passing frequency. It shows that the splitter blades do not give exactly the same upstream imprint on the pressure distribution as the full blades. A harmonic corresponding to the total number of runner blades is found at $31.2n$. The corresponding experimental peak is at $29.6n$. The pressure on the blade surface shows a strong oscillation with a frequency of $29.1n$. The corresponding experimental peak is at $27.7n$. This frequency corresponds to the blades passing the 28 guide vanes. A series of peaks on the blade surfaces located between $17.8n$ and $18n$ which is measured experimentally is not found in the simulations. On the other hand, the frequency located at $62.3n$, in the vane-less space and in the draft tube, is found in the numerical results but is not present in the measurements. Figure 16 shows that axial torque oscillations occur with the main peak at $31.2n$, corresponding to the total numer of runner blades, and a small peak at $15.6n$, corresponding to the full blade passage. An additional peak is observed at $62.3n$, corresponding to the high-frequency pressure fluctuations predicted at all sensor locations, which are not observed experimentally.

The frequency spectrum of the pressure fluctuations at part load is presented in Figure 17. In the vaneless space, the passing frequency of the full blades is observed at $15.4n$, corresponding to the experimentally observed $15n$. The frequency corresponding to the total number of blades is found at $30.77n$, which corresponds to the experimentally observed $30n$. On the blade surface, the guide vane passing frequency predicted at $28.7n$, corresponding to the experimentally observed $28n$. The experimental data shows a second peak at $29.55n$, which is not observed numerically. The experimental data also show a strong peak at $44.3n$. A tendency of such a peak is predicted numerically, but shifted to $46.1n$. The draft tube probes show the blade passing frequency at $15.4n$, experimentally observed at 14.8. The draft tube frequency corresponding to the total number of runner blades is predicted at $30.8n$, which corresponds to two experimental peaks, at $29.55n$ and $30n$. The numerically predicted frequency of $46.1n$ is experimentally measured at $44.3n$. A low frequency oscillation in the draft tube is observed at $0.27n$ in the experiments, while the numerical results show one at $0.5n$. However, the peak is very weak and no clear single frequency is present. This is consistent with the observation made by Dörfler *et al.* [20, pp. 40-41], that the stable vortex rope is replaced by random pulsations at very low part load. Figure 18 again shows that axial torque oscillations occur at $30.71n$. There is as well a harmonic at $92.13n$.

Figure 19 shows the frequency spectrum of the simulated pressure fluctuations at high load.

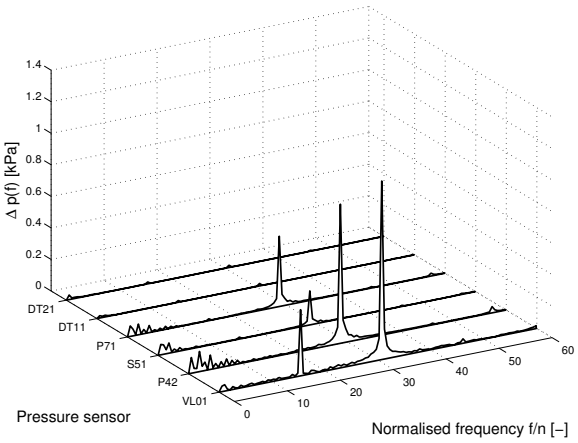

Figure 17: Frequency spectrum of the pressure fluctuations at part load, normalised by the runner rotation frequency. Unsteady k-ε.

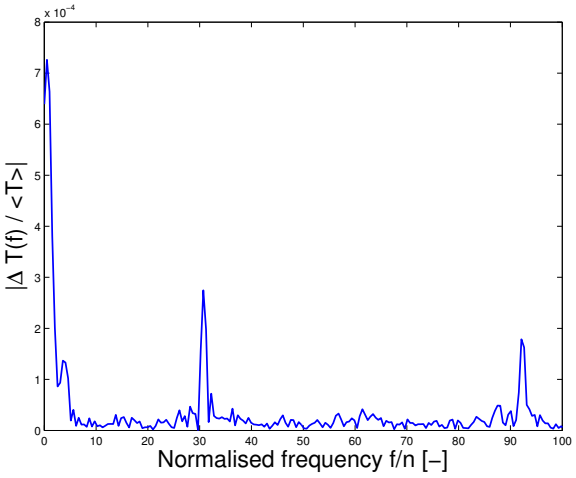

Figure 18: Frequency spectrum of the axial torque at part load, normalised by the runner rotation frequency. Unsteady k-ε.

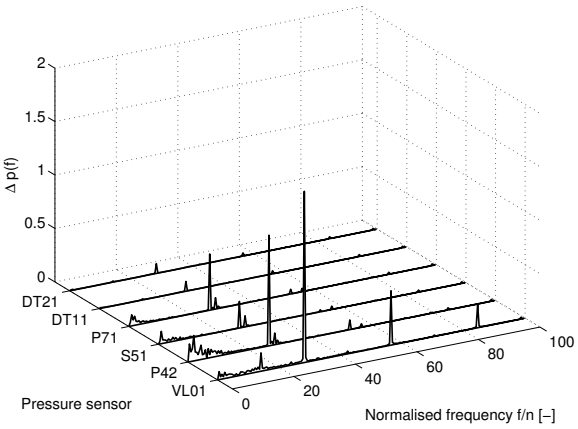

Figure 19: Frequency spectrum of the pressure fluctuations at high load, normalised by the runner rotation frequency. Unsteady k-ε.

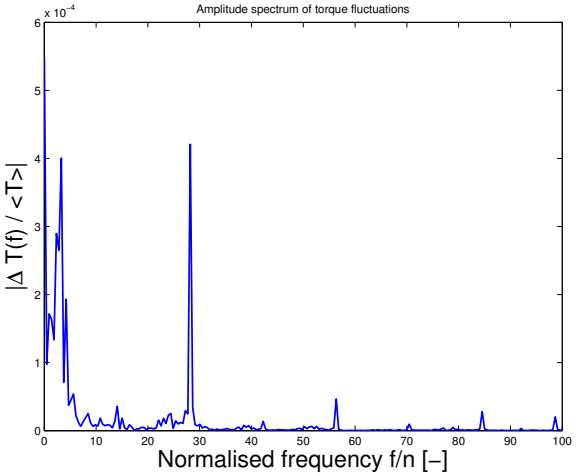

Figure 20: Frequency spectrum of the axial torque at high load, normalised by the runner rotation frequency. Unsteady k-ε.

In the vaneless space, the frequencies corresponding to the full blade passage and the total runner blade passage are shifted from their expected values of $15n$ and $30n$ to $14.1n$ and $28.2n$, respectively. These frequencies are not observed experimentally. The frequency of the total number of runner blades is present in the draft tube at $28.2n$. On the blade surface, the guide vane passing frequency is at $26.3n$, while two experimental peaks are observed at $28n$ and $30n$. The experimental frequencies at $48.7n$ are not present in the simulations. On the other hand, the peak at $56.4n$ in the vane-less space is not present in the experimental results. Figure 20 shows that the axial torque fluctuations have a main peak at $28.3n$, which is the same as the most significant pressure fluctuation. A minor peak is observed at $14.1n$, which is also observed in the pressure data.

4. Conclusions

Steady-state and unsteady numerical simulations are performed at three operating conditions of the Tokke high-head Francis turbine model, using several turbulence models. The steady-state simulations use a mixing plane, and the unsteady simulations use a sliding GGI interface, for the coupling of the stationary and rotating parts of the domain. The steady-state simulations use a multiple frames of reference approach, and the unsteady simulations use a rotating mesh, to represent the runner rotation. A single blade passage of the guide vanes and runner blades is used in the steady simulations, together with a cyclic GGI, while the unsteady simulations include all the blades. The steady simulations have an inlet just before the guide vanes, while the unsteady simulations have the inlet before the spiral casing. All simulations have the outlet after the draft tube. Most of the numerical predictions show reasonable agreement with the experimental data, with exceptions as summarized below.

The hydraulic efficiency predictions of the unsteady simulations closely correspond to those of previously published simulations by other authors using a proprietary CFD code. The error compared with the experimental data is 1.16% at the design point, 2.27% at high load, and 10.67% at part load. The similar behaviour of the present and previous numerical results suggest that there is a systematic error in the case description, the mesh, or the common methods. All of those were similar in the present and the previously published study. The steady-state results do however yield much higher errors in the prediction of the hydraulic efficiency. The losses in the spiral casing are not included in the steady-state simulations, and the choice of inlet conditions just before the guide vanes should be revised to investigate their effects on the predicted hydraulic efficiency. This is the main deficiency of the steady-state results. If this deficiency is removed, the fast steady-state results are as accurate as the time-consuming unsteady results as long as it is the mean flow features and engineering quantities that are of interest.

The overall behaviour of the numerically predicted static pressure distributions is very similar to the experimental ones. A main source of difference is related the region between the trailing edges of the runner blades and the first measurement point in the draft tube. The effect of the mesh resolution and mesh quality in that region should be further investigated. The presently used turbulence models are quite similar in nature, and they may not be able to correctly capture the effects of turbulence in that region. At high load, the draft tube pressure recovery is predicted different than the experimental one by all simulations, including the previously published simulation.

The velocity distributions are predicted reasonably similar to the experimental ones at part load and high load. At those conditions it is mainly the width and strength of the recirculation region below the hub that differs between models and compared to the experimental distributions. Even furher convergence of the steady-state results, and longer simulation times for the unsteady results, should be considered to verify that the flow is indeed fully developed in that region. At the best efficiency condition also the tangential velocity distribution shows an unexpected and unexplainable large discrepancy compared to the experimental one. This behaviour is the same for all the turbulence models used in the present work, and it is one of the top priorities for further investigations.

A Fourier analysis shows that the unsteady simulations are capable of resolving the most important pressure and torque fluctuations. However, there is a slight frequency shift compared to the experimental results and the expected values. The accuracy of the frequency spectrum could be improved by choosing a smaller time step and increasing the observation period.

All turbulence models used in the present work are part of the FOAM-extend CFD code except for the linear EARSM model, which is implemented in the present work. It shows similar behaviour as the other models. A main difference is that it gives a narrower and stronger recirculation region below the hub. The implementation should be further verified before any major conclusions can be drawn, and the full EARSM model should as well be investigated.

Acknowledgements
The authors would like to thank the Swedish national infrastructure for computing (SNIC) and the Chalmers centre for computational science and engineering (C^3SE) for providing support and the computational resources for this work. Professorn Nilsson is financed by the Swedish Hydro Power Center (SVC). SVC was established by the Swedish Energy Agency, Elforsk, and Svenska Kraftnät together with Luleå University of Technology, the Royal Institute of Technology, Chalmers University of Technology, and Uppsala University. Our thanks go also to Ardalan Javadi, who contributed with his experience. Furthermore, the efforts made by Martin Beaudoin and Prof. Hrvoje Jasak for the continuous improvement of FOAM-extend for turbomachinery applications as well as the fruitful discussions are much appreciated.

References
[1] Nicolet C 2007 *Hydroacoustic modelling and numerical simulation of unsteady operation of hydroelectric systems* Ph.D. thesis École polytechnique federale de Lausanne
[2] Shingai K, Okamoto N, Tamura Y and Tani K 2014 *J. Fluids Eng.* **136** 071105
[3] Keck H and Sick M 2008 *Acta Mech.* **201** 211 – 229
[4] Nicolet C, Zobeiri A, Maruzewski P and Avellan F 2011 *I. J. Fluid Mach. and Syst.* **4** 179 – 190
[5] Nilsson H 2006 *23th IAHR Symp. on Hydr. Mach. and Syst.*
[6] Petit O 2012 *Towards full predictions of the unsteady incompressible flow in rotating machines, using OpenFOAM* Phd thesis Department of Fluid Dynamics, Chalmers University of Technology Göteborg, Sweden
[7] Javadi A 2014 *Time-accurate Turbulence Modeling of Swirling Flow for Hydropower Application* Licentiate thesis Department of Fluid Dynamics, Chalmers University of Technology Göteborg, Sweden
[8] Beaudoin M, Nilsson H, Page M, Magnan R and Jasak H 2014 *27th IAHR Symp. on Hydr. Mach. and Syst.* (Montreal, Canada)
[9] Page M, Beaudoin M and Giroux A M 2011 *I. J. Fluid Mach. and Syst.* **4** 161–171
[10] Petit O, Bosioc A I, Nilsson H, Muntean S and Susan-Resiga R F 2010 *25th IAHR Symp. on Hydr. Mach. and Syst.* **12** 012056
[11] Zhang H and Zhang L 2012 *Procedia Eng.* **31** 156 – 165
[12] Susan-Resiga R, Muntean S, Stein P and Avellan F 2009 *I. J. Fluid Mach. and Syst.* **2** 295 – 302
[13] Maruzewski P, Hayashi H, Munch C, Yamaishi K, Hashii T, Mombelli H P, Sugow Y and Avellan F 2010 *IOP Conf. Ser.: Earth Environ. Sci.* **12** 1–9
[14] Wu Y, Liu S, Wu X, Dou H, Zhang L and Tao X 2010 *IOP Conf. Ser.: Earth Environ. Sci.* **12** 012004
[15] Trivedi C, Cervantes M J, Gandhi B and Dahlhaug O G 2013 *J. Fluids Eng.* **135** 111102
[16] IEC TC/SC 4 1999 *IEC 60193 Hydraulic turbine, storage pumps and pump-turbines - Model acceptance tests* (Geneva, Switzerland: International Electrotechnical Commission)
[17] Beaudoin M and Jasak H 2008 *Open Source CFD International Conference 2008* (Berlin, Germany)
[18] Wallin S 2000 *Engineering turbulence modelling for CFD with a focus on explicit algebraic Reynolds stress models* Phd thesis Royal Institute of Technology (KTH) Stockholm, Sweden
[19] Gyllenram W and Nilsson H 2008 *J. Fluids Eng.* **130** 051401
[20] Dörfler P, Sick M and Coutu A 2013 *Flow-Induced Pulsation and Vibration in Hydroelectric Machinery* (London: Springer)